Research Article | Vol. 30, No. 22 / 24 Oct 2022 / Optics Express 40557
Optics EXPRESS

O_2 based resonantly ionized photoemission thermometry analysis of supersonic flows

WALKER MCCORD,[1] MARK GRAGSTON,[1,2] DAVID PLEMMONS,[3] AND ZHILI ZHANG[1,*]

[1]Department of Mechanical, Aerospace, and Biomedical Engineering, The University of Tennessee -Knoxville, Knoxville, Tennessee 37996, USA
[2]Department of Mechanical, Aerospace, and Biomedical Engineering, University of Tennessee Space Institute, Tullahoma, Tennessee 37388, USA
[3]National Aerospace Solutions, Arnold AFB, Tennessee 37389, USA
*zzhang24@utk.edu

Abstract: Characterization of the thermal gradients within supersonic and hypersonic flows is essential for understanding transition, turbulence, and aerodynamic heating. Developments in novel, impactful non-intrusive techniques are key for enabling flow characterizations of sufficient detail that provide experimental validation datasets for computational simulations. In this work, Resonantly Ionized Photoemission Thermometry (RIPT) signals are directly imaged using an ICCD camera to realize the techniques 1D measurement capability for the first time. The direct imaging scheme presented for oxygen-based RIPT (O_2 RIPT) uses the previously established calibration data to direct excite various resonant rotational peaks within the S-branch of the $C^3\Pi$, $(v=2) \leftarrow X^3\Sigma(v'=0)$ absorption band of O_2. The efficient ionization of O_2 liberates electrons that induce electron avalanche ionization of local N_2 molecules generating $N_2{}^+$, which primarily deexcites via photoemissions of the first negative band of $N_2^+(B^2\Sigma_u^+ - X^2\Sigma_g^+)$. When sufficient lasing energy is used, the ionization region and subsequent photoemission signal is achieved along a 1D line thus, if directly imaged can allow for gas temperature assignments along said line; demonstrated here of up to five centimeters in length. The temperature gradients present within the ensuing shock train of a supersonic under expanded free jet serves as a basis of characterization for this new RIPT imaging scheme. The O_2 RIPT results are extensively compared and validated against well-known and established techniques (i.e., CARS and CFD). The direct imaging capability fully realizes the technique's fundamental potential and is expected to be the standard of implementation going forward. The direct imaging capability can play instrumental roles in future scientific studies that rely upon acute characterization of thermal gradients within a medium that cannot be easily resolved by a point. Furthermore, the removal of the spectrometer greatly reduces the cost, complexity, and optical alignment associated with prior RIPT measurements.

1. Introduction

For decades, the thermal gradients of supersonic flows have been studied due to the many areas of interest in which they can arise, from natural events to daily life, and critically within challenging engineering environments. In the exhaust plumes of high-speed aircraft and rockets, the thermal gradients within the shock structures are critical as it affects the thermal signature, jet noise, and screech of the engines [1–5]. Critical information of thermal gradients is needed for mixing, fuel ignition, and combustion instabilities within supersonic air-breathing combustors [6–8]. Under expanded supersonic free jets have even been used to model the flow dynamics of a volcanic ash-cloud ejecting from a vent (volcano) into the atmosphere [9]. A recent rise of hypersonic and high-supersonic research coupled with aggressive developments in computational power has paid significant attention to thermal protection, since thermal gradients present in the boundary layer

#471021 https://doi.org/10.1364/OE.471021
Journal © 2022 Received 22 Jul 2022; revised 14 Sep 2022; accepted 16 Sep 2022; published 18 Oct 2022

Optics EXPRESS

of the supersonic flow becomes critically important as surface heating dramatically rises due to combined effects of transition, turbulence, and increased skin frictions at very high speeds [10–16].

The high gas velocities associated with hypersonic or high-supersonic flow regimes limit the applicability of conventional flow characterization methods, as physical disturbances of sufficient strength can propagate downstream and alter flow phenomena which can invalidate measurements taken within the Region of Interest (ROI) [17,18]. Non-intrusive thermometry techniques that can serve as a mean of characterization tools are thus needed for physical understanding of the supersonic flow transition, turbulence, aerodynamic heating and control, and calibration and validation of computational models [10,19,20]. Some current optical thermometry techniques include Planar Laser Induced Fluorescence (PLIF), Tunable Diode Laser Absorption Spectroscopy (TDLAS), Filtered Rayleigh Scattering (FRS), and Coherent Anti-stokes Raman Spectroscopy (CARS) [10,21–27], which all have various limitations. For low-enthalpy, high-speed flows similar to the ones presented in this work, PLIF has to rely on tracer molecules, such as nitric oxide or an aromatic molecule that must be seeded into the flow which can negatively impact flow chemistry and dynamics [21,23,28]. TDLAS suffers from path-integration effects that can limit resolving ability for small ROI's [29–31]. CARS is a non-intrusive technique that does not require flow seeding and is non-path integrated, historically making it an attractive option for thermometry measurements [10,22,32–34]. There are current efforts to examine and improve the feasibility of 1D/2D CARS measurements in lower enthalpy flows that have seen varying levels of success [35–37]. Recently, 1D CARS measurements through an under expanded free jet that is similar to the one in this work was able to achieve accurate temperature fits across a 6mm line length [38]. However, CARS is susceptible to misalignment in high-noise environments, and requires the use of multiple lasers and complex optical delay paths to achieve precise spatiotemporal overlapping of the beams [22].

O_2 RIPT is a relatively new technique that was realized through an in-depth study and calibration that laid the ground work for the technique to easily be implemented by outside researchers for temperatures between 180 to 460 Kelvin [1,39–43]. While the aforementioned work alludes to the techniques ability to enable 1D measurements without the use of a spectrometer; no such effort was demonstrated or presented within the results. In this work, O_2 RIPT techniques 1D ability is realized via direct imaging for the first time. A bandpass filter is used to remove contributions that are not relevant to the first negative band of nitrogen, $N_2^+(B^2\Sigma_u^+ - X^2\Sigma_g^+)$, thus allowing only temperature sensitive photoemissions to be captured along a 1D ionization line. A shock train generated aft of the nozzle exit of a moderately under expanded supersonic free jet is an environment that presents dynamic thermal gradients, turbulence mixing, pressure fluctuations, and various other fluid phenomena associated with the reciprocating "barrel-like" structures. This presents a challenging yet ideal environment for establishing O_2 RIPT's 1D capability as it will allow quantification of the technique's pressure/signal dependence, temperature assignment accuracy, and spatial resolution.

2. Theory

The core idea behind the O_2 RIPT technique is by utilizing an O_2 (2 + 1) REMPI scheme, that is two photons excite an oxygen molecule to an intermediate state followed by the absorption of an additional photon to ionize. By specifically selecting wavelengths within a resonant absorption band of O_2, focused laser light can induce a 1D weakly ionized plasma line. The REMPI structure and underlying physics upon which O2 RIPT is enabled has previously been detailed in literature [1]. For coherency, a brief summary is given here. First specifically chosen rotational lines within the S-branch of the $C^3\Pi, (v = 2) \leftarrow X^3\Sigma(v' = 0)$ band of O_2 are resonantly excited and ionized via a frequency doubled dye laser with sufficient energy to create a localized region of ionized O_2 molecules, shown by Eq. (1). This rotational branch was selected due to spectral

Optics EXPRESS

distinctness and relevant population distributions for the thermal conditions within the expanded jet test environment.

$$O_2 + 3h\nu_{REMPI} \rightarrow O_2^+ + e^- \tag{1}$$

The resulting photoelectrons are then accelerated by the remaining laser pulse via inverse Bremsstrahlung absorption to induce photoelectron avalanche ionizations and electron-impacted collisional excitation of N_2, given by Eq. (2).

$$N_2^+ : N_2 + e^- + \hbar\nu \rightarrow N_2^+ + 2e^- \tag{2}$$

The recombination of electrons and molecular nitrogen ions produces photoemissions of the first negative band of $N_2^+(B^2\Sigma_u^+ - X^2\Sigma_g^+)$, or further decay by the first positive band of N_2 [44]. Expressed by Eq. (3), and Eq. (4).

$$N_2^+(B) \rightarrow N_2^+(X) + \hbar\nu_{1^-} \tag{3}$$

$$N_2^+ + e^- \rightarrow N_2(B) \rightarrow N_2(A) + \hbar\nu_{1^+} \tag{4}$$

The resulting photoemissions from the N_2^+ first negative band are at three distinct spectral peaks (Δv_0, 390 nm; Δv_2, 425 nm; Δv_1, 430 nm), resulting from the $1 \rightarrow 0, 2 \rightarrow 1$, and $1 \rightarrow 1$ transitions, respectively. These spectral emissions make up the thermometry signal. Fundamentally, RIPT measurements are enabled from two unique relationships; (1) the electron impacted excited N_2^+ and resulting photoemissions within the first negative band share a direct relationship with the specifically excited rotational line strength within the O_2 S-rotational branch. (2) The two-photon transitional line strengths ($T^2_{f,g}$) at various resonant frequencies either exhibits temperature sensitivity or insensitivity and directly effects the strength in generated photoemissions. The previous calibration study of O_2 RIPT found that the generated photoemission signal strength (i.e., specifically those of the first negative branch of N_2) is directly related to the Boltzmann distribution in the ground state. Thus, by probing various rotational peaks of O_2 a linear regression fit can be applied to the captured signals to statistically assign a gas temperature. Furthermore, the calibration study identified four ideal rotational peaks for excitation across temperature ranges that varied between 180 to 460 Kelvin and that allow accurate statistical weighted gas temperature assignments [1].

Based off the results of the previously published calibration study for O_2 RIPT, resonant absorption wavelengths for the 180 and 293 Kelvin temperature setpoints were selected for excitation in this study [1]. These wavelengths were selected based off the expected temperatures generated within the shock train features. A feature that was found from the O_2 calibration experiment is the ideal resonant absorption peaks that enable accurate gas temperature assignment for both 180 and 233 Kelvin environments are maintained. Thus, it can be inferred that the population distributions below 233 Kelvin do not shift dramatically; inferring the 180 and 293 Kelvin wavelengths should be sufficient for complete thermal characterization. The rotational peaks wavelengths and corresponding properties for both the 180 and 293 Kelvin are tabulated in Table 1.

Using the values from Table 1, the frequency doubled dye laser was tuned to each resonant wavelength for corresponding thermal sets, and the resulting photoemissions were captured and related to temperature using Eq. (5). Where, E_{g_n} is the ground state energy, I_{λ_n} is the emission intensity at a laser excitation wavelength "n", T is the medium temperature, and k_B is the Boltzmann constant.

$$-\frac{1}{k_B T} \propto log\left(\frac{I_{\lambda_n}}{T^2_{f_n,g_n}}\right)/E_{g_n} \tag{5}$$

To summarize, the previous calibration study of the O_2 $C^3\Pi, (v = 2) \leftarrow X^3\Sigma(v' = 0)$ absorption band found that through direct stimulation via laser emission generated N_2^+ photoemissions

Optics EXPRESS

Table 1. Laser wavelengths for O_2RIPT temperature determination and corresponding spectral properties.[a]

Excitation wavelengths for 180 Kelvin			
λ *nm*	J'	G_1 cm^{-1}	$T^{(2)}_{f,g}$
286.99	11	190.74	7.70
287.18	7	81.57	5.66
287.26	5	44.20	4.62
287.34	3	18.33	3.50
Excitation wavelengths for 293 Kelvin			
λ *nm*	J'	G_1 cm^{-1}	$T^{(2)}_{f,g}$
286.51	19	546.62	12.73
286.65	17	440.49	10.72
286.78	15	345.79	9.72
287.09	9	130.42	6.69

[a]Here J' is the rotational quantum number for the ground state, G_1 represents hyperfine structure in the ground state, and $T^{(2)}_{f,g}$ is the two-photon transition probability.

from locally available nitrogen in standard air. These photoemissions were found to be directly related to the rotational line strength in the O_2 absorption band and thus, are representative of the Boltzmann distribution of oxygen in the ground state. Various rotational peaks were identified which, through direct stimulation, allows a gas temperature to be statistically assigned. This work expands upon the previous by capturing the resulting signal with an ICCD camera where the areas of the image that contain signals serves as inputs to statistically assign a gas temperature on a pixel-by-pixel basis. This enables the direct imaging capability along a line of generated emissions.

3. Experimental setup

O_2 RIPT setup

The setup for O_2 RIPT measurements is relatively straightforward and has minimal optical alignment, a general rendering of the setup is shown in Fig. 1. The second harmonic of an Nd:YAG laser (Spectra Physics Pro – 290) with a pulse width of 10 ns, repetition rate of 10 Hz, and approximately 1 Joule per pulse (J/pulse) lasing energy was used to pump a dye laser (Sirah PrecesionScan) which utilized a mixture of Rhodamine 590 and Rhodamine 610 to yield high energy conversions near 574 nm with an 0.06 cm^{-1} linewidth. The output of the dye laser was frequency doubled via a look-up table system (Sirah Tunable Frequency Conversion unit), to produce ultraviolet (UV) light and maintain high conversion efficiencies across the entire absorption range. The UV beam has nominal per pulse energies of approximately 30 mj/pulse within the $C^3\Pi, (v = 2) \leftarrow X^3\Sigma(v' = 0)$ band of O_2. The UV beam was focused using a + 300 spherical fused silica lens, generating a photoemission line of approximately 100 mm in length. It should be noted, due to quenching effects, only half of the generated line was useable for temperature measurements. The photoemission line was positioned down the centerline axis of the jet and occupied the region from the nozzle exit to approximately 50 mm downstream. The length of the line was sufficiently long enough to capture all shock-structures within the jet until fully-developed flow had been reached. The jet nozzle exit diameter is 3.175 mm. The fluorescence line emissions were captured via an intensified scientific camera (PI-MAX4 1024f) where sensor binning was implemented that resulted in an effective sensor size of (512×512 pixels). A 2mm thick BG3 Schott's glass (UV-blue) bandpass filter was positioned in-front of

Optics EXPRESS

the imaging lens to filter out any contributions from laser, scattered, or background light that is outside of the first negative band of N_2. Details regarding the geometry and design of the supersonic jet nozzle can be found in Supplement 1, specifically in Fig. S1.

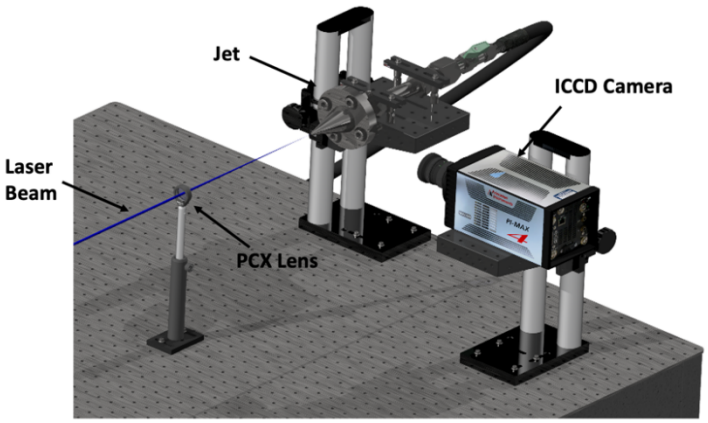

Fig. 1. O_2 RIPT experimental setup for jet shock-train thermal characterization.

ps-CARS setup

To validate photoelectron induced emissions measurements, ps-CARS (pico-second vibrational Coherent Anti-Stokes Raman Scattering) was performed at various locations downstream of the nozzle exit. The ps-CARS system used here is owned and operated by the advanced diagnostic group at Arnold Engineering Development Complex (AEDC) and has been demonstrated to achieve vibrational N_2 gas temperature measurements in the exhaust of a J85 turbojet engine [45]. Furthermore, the system has been used for measurements in low-enthalpy, low-density environments of the hypersonic Tunnel 9 facility, thus making it well suited for comparison to O_2 RIPT in this instance. The experimental setup is shown in Fig. 2.

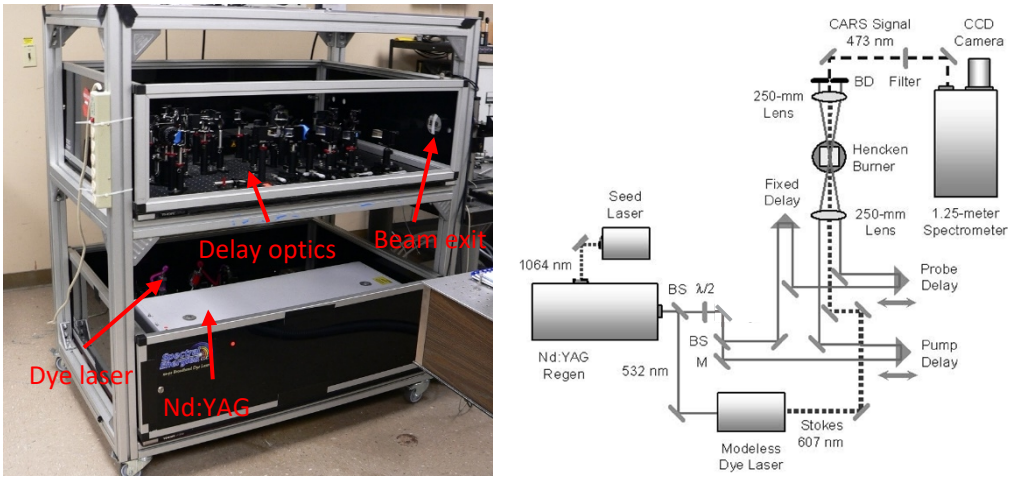

Fig. 2. AEDC transportable ps-CARS setup and optical layout for the BOXCARS geometry.

The system consists of a 100-ps laser (Ekspla SL234, 532 nm, approximately 0.2 cm^{-1}) at 106 mJ/pulse energy, which was used to pump a custom built, tunable ps-capable dye laser (607 nm) with FWHM of 135 cm^{-1} and pulse duration of 115 ps that yielded maximum outputs of 5

Optics EXPRESS

mJ/pulse lasing energy. The energies for the pump, probe, and Stokes beam were measured to be approximately 5.6 mJ, 5.6mJ, and 4.7mJ respectively. The system and all required optics are housed on two 4×3-foot breadboards that are mounted to an aluminum t-slot frame that allows for transportation of the system with minimal disturbance to the optical alignment. The three output beams were focused using a + 300 mm fused silica lens. The focal region of the lens was positioned on the centerline of the jet. The jet assembly, shown in Fig. 3, was secured to a linear translation stage to provide precise control over measurement locations. A narrow bandpass filter (Semrock, LD01-473/10-25.4) was used to remove any background scattering from the anti-Stokes signal beam, which was then dispersed via a 1 m spectrometer (Jobin Yvon Model SPEX 1000M) that utilized a 2400 groove/mm grating. The signal was collected with a CCD camera (Andor Technologies Model DU 440BU).

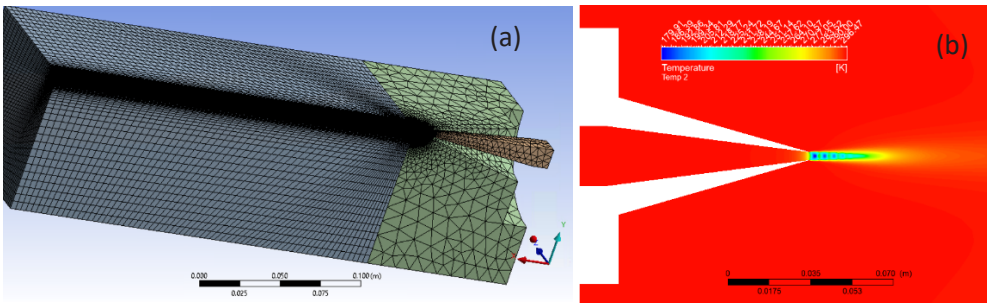

Fig. 3. 3D mesh for ¼ of the jet geometry (a) and CFD generated temperature map (b).

CFD simulation

To better validate the measurements, a simple RANS-based simulation of the supersonic jet was done using ANSYS Fluent CFD software. Since the free jet used in this study is axisymmetric, only a quarter slice of the 3D nozzle geometry was used in the meshing parameters to reduce computational time and energy required. Structured meshing was used beyond the nozzle exit to better accommodate viscous effects, while an unstructured meshing was used elsewhere. Figure 3(a),(b) depicts the meshing used for the computations. Region 1 meshing had a mesh sizing restriction of 2 mm and Region 3 had a 0.1 mm sizing. Region 2b was also subject to mesh sizing of 0.1 mm. For each case, program-controlled matching of the regions was allowed. The RANS computations utilized the Spalart-Allmaras turbulence model [46]. The inlet boundary condition for the jet was specified as a 220.6 kPa pressure with temperature of 300 K and reverse flow was prevented. The working gas was assumed to be ideal air, with the Sutherland viscosity formula used for determining viscosity during the computations. Far-field pressure outlet conditions were used for the non-symmetry walls with exception of base plane, which was modeled as a solid wall for simplicity.

4. Results and discussions

O_2 RIPT

The raw O_2RIPT emission images that resulted from direct stimulation of the wavelengths that correspond to the 180 Kelvin temperature range that were established in the aforementioned calibration study are shown in Fig. 4(a) and Fig. 4(b) for flow off and flow on cases, respectively. The images corresponding to 293 Kelvin wavelengths are shown by Fig. S2 in Supplement 1. The raw O_2 RIPT emission images shown in Fig. 4 are 20-shot averages and background subtracted to minimize laser energy fluctuations and background artifacts. The O_2 RIPT signal intensity is affected by the number density of local nitrogen molecules; thus, it is possible to resolve the shock-train structures locations downstream of the nozzle exit by taking a line average across the

Optics EXPRESS

emission image. This is shown in Fig. 4(d). The peaks and valleys within the averaged signal represent reflected shocks and expansion fans, respectively. Finally, the line average of the flow off cases is shown for coherency in Fig. 4(c).

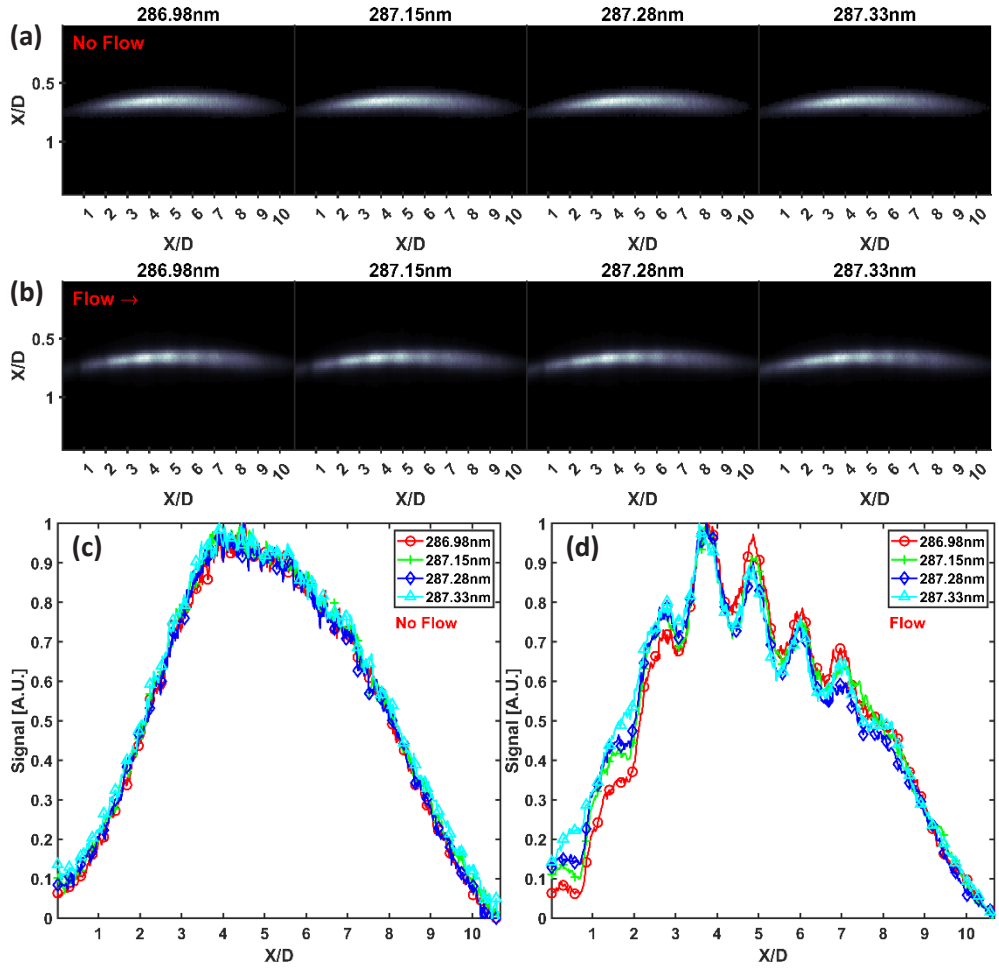

Fig. 4. 180 Kelvin captured photoemissions for (a) no flow, and (b) flow cases. Line average profiles down the centerline of the emissions for (c) no flow, and (d) flow.

Corrected images are taken and stacked into a three-dimensional (3D) array, which allows for the intensity in each pixel to be processed using the aforementioned equations and ensures that pixel locations are maintained for each image set. The post-processing code computes the Boltzmann plots and assigns temperature through a statistical fit of those plots at a pixel-by-pixel level. Analyzing the images in this way allows each pixel to represent a unique gas temperature measurement. Furthermore, since the processing is occurring for individual pixels, this automatically places the upper limit on the spatial resolution of O_2 RIPT technique for this experiment which was found to be 50μm. The accuracy of O_2 RIPT technique is heavily dependent upon correctly selecting the resonant O_2 peaks that demonstrate high linearity within a specified range of gas temperatures. Since the gas temperature through the supersonic moderately under-expanded jet dramatically fluctuates as it passes through the complex shock-interactions aft of the nozzle exit plane, the post-processing code used the coefficient of determination (R^2) in each pixel to determine which temperature-wavelength set should be used (i.e., those pertaining

Optics EXPRESS

to 180 or 293 Kelvin). This method resulted in O_2 RIPT measurements of high accuracy and demonstrated sufficient thermal sensitivity to resolve the thermal gradients present throughout the shock structures and into fully developed flow region as depicted in Fig. 6. To find the "total" error of the O_2 RIPT measurement for this experiment, the error associated with the linear regression fit (i.e., the statistical fit) and the induced SNR error were taking into account. The associated experimental error was found to be approximately ±12 K. It should be noted, as long as the environmental conditions are maintained across all probing wavelengths and provide sufficient photoemission intensity, then the thermometry capabilities are unaffected by quenching or pressure rates for low enthalpy mediums.

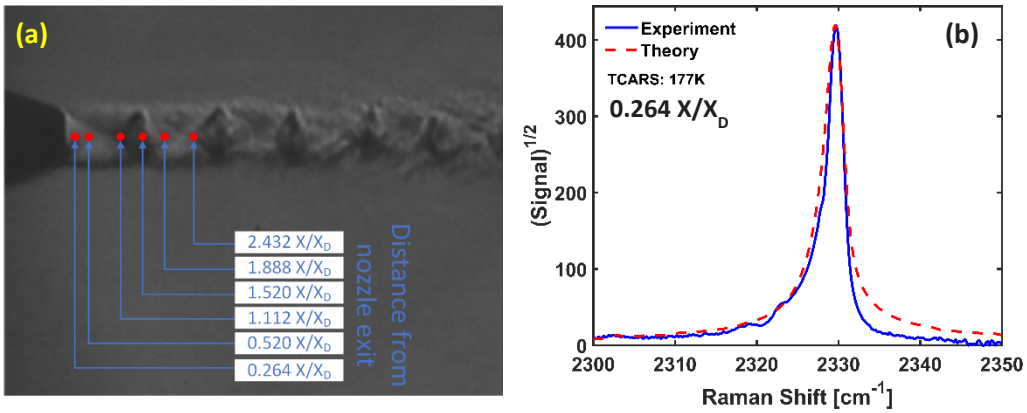

Fig. 5. CARS measurement locations with relation to free jet nozzle exit overlaid with schlieren (a). CARS experimentally obtained spectrum and CARSFT fitted spectrum for temperature determination at 0.264 X/X_D location relative to nozzle exit (b).

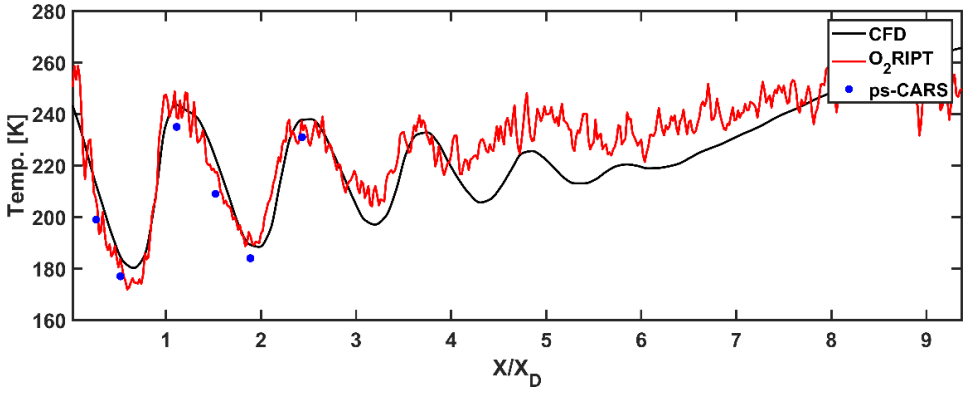

Fig. 6. CFD, O_2 RIPT, and ps-CARS temperature measurements within the under expanded supersonic jet shock train depicting good agreement across all techniques.

Additionally, it was found that with sufficient laser power (>28 mj/pulse), sufficient ionization is generated within the region of the laser beam such that areas that extend past the beam waist are subsequently ionized as well. This enabled a temperature "map" as depicted in Supplement 1 Fig. S3(*a*). Additionally, CFD predicted total gas temperature is shown in Fig. S3(*b*) for comparison. The region for which the processing occurred was confined to areas of sufficient emission intensity that yielded SNR values (>10) to maintain accuracy.

ps-CARS measurements

Optics EXPRESS

To compare the sensitivity and accuracy of O_2 RIPT thermometry, ps-CARS spectra were recorded at six different locations of interest that were within the shock train of the under expanded supersonic free jet. These locations were identified as points of interest, as they were regions of either dramatically decreasing or increasing gas temperatures and are depicted in Fig. 5(a). The ps-CARS spectra were acquired at a repetition rate of 10 Hz. The free jet flow was initiated and allowed to run for a few seconds to ensure shock-train stability was reached between collections. The ps-CARS spectra signal was a 30-shot average acquired over 100μs exposures and background subtracted. Average signal levels were approximately 120,000 counts with an SNR of approximately 4,000. To extract thermodynamic information from the experimentally obtained spectra, theoretically spectra was generated by the N_2 spectral modeling program CARSFT [47] in an iterative least-squares fitting manner. The experimentally acquired spectra and corresponding CARSFT fits with the predicted vibrational temperature measurements are shown for the first measurement location in Fig. 5(b); fits corresponding to all locations can be found within Supplement 1 in Fig. S4.

Conventionally, CARSFT is best utilized in high enthalpy environments where there exists higher vibrational modes and greater structure that enables easier fitting for thermodynamic information. Due to the cold gas temperatures within the shock train, the captured spectra are sparse in structure only having a single observable peak at approximately 2330 cm^{-1} that is from the Q-branch transition between vibrational levels $1 \rightarrow 0$. This lack in structure makes fitting an accurate temperature increasingly difficult compared to high-enthalpy environments. This is not to say it is infeasible, as previous CARS based measurements have been conducted in various low-enthalpy environments [48,49], such as freestream measurements of Mach 14 flow in the Tunnel 9 facility (i.e., $T_\infty \propto 51K$) [22]. For this experiment, the CARS probe has a pulse width of ~100 picoseconds that is not capable of yielding pressure-insensitive temperature measurements. This complicates the fitting aspect due to multiple reasons and is extensively discussed within Supplement 1. To succinctly put it, a numerical approach calculated theoretical pressure values through the shock train, which were used to create a range of possible pressures at each measurement location. The calculated pressure values were checked against CFD pressure values obtained down the centerline of the shock train and depicted in Fig. S7. The calculated pressure range served as inputs to the CARFT program establishing upper and lower bounds that served as inputs to an iterative least-squares fit which was applied to the respective experimentally obtained spectra. The code was allowed to run through potentially hundreds of iterations until a best fit was found. This method yielded sufficient temperature predictions that when compared to the O_2 RIPT measurements shows very good agreement as shown in Fig. 6.

O_2 RIPT, ps-CARS, and CFD

A comparison of the CFD, O_2 RIPT, and ps-CARS temperature measurements is shown in Fig. 6. The agreement between the various methods is good and shows promising capabilities for O_2 RIPT based measurements. The ps-CARS predicted temperature better aligns with the O_2 RIPT measured temperature than the CFD results. This is expected as the CARS and O_2 RIPT are measurements of the vibrational N_2 temperatures and the CFD is a total temperature measurement. The O_2 RIPT and CFD data align well through the shock-train, but near $X/D = 4$ diverge slightly. The indicated O_2 RIPT thermal line measurement displayed in Fig. 6 is achieved by taking a four-pixel tall average down the centerline of the emissions. A small temperature discrepancy between O_2 RIPT measurements and CFD does not occur until the flow is nearing its fully-developed region, thus it is believed that the O_2 RIPT measurements yield a higher temperature measurement within the fully developed region to be due to mixing and other viscous fluid interactions that are not fully accounted for within the CFD's turbulence model.

Optics EXPRESS

5. Conclusions

In summary, a moderately under expanded supersonic free jet with a focus on the ensuing shock-train formations aft of the nozzle exit plane is rigorously analyzed through multiple methods to serve as a means of validation of O_2 RIPT technique and its capabilities. Furthermore, this is the first study to realize O2 RIPT's true 1D potential via direct imaging of the generated photoemissions, thus providing key diagnostic info for that was still unknown. The complex excitation and energy transfer mechanisms that are involved with O_2 RIPT technique inherently induce constraints to the properties of the working medium. The emission from the first negative band of N_2^+ directly results from electron impact excitation of local nitrogen molecules that is procured through electron avalanche ionization of resonantly excited and ionized O_2. Thus, O_2 RIPT fundamentally relies upon strong stochastic effects of the electron avalanche ionization within the locally ionized region of the focused laser emission. Special care must be taken into the actual formation of the ionization region and selection of the lens to focus the laser emission. As regions of very intense laser energy induces ionization and results in a plasma density with greater frequency than the incoming light frequency, back propagation and back scattering of the laser emissions will occur creating regions of more and less dense plasma that could impact the N_2^+ photoemission Boltzmann dependence.

Furthermore, there will exist some time delay between resonantly exciting O_2 and the N_2^+ photoemission. It has been previously studied and found in literature that this delay is approximately 80 picoseconds for standard temperature and pressure [50]. Within the ionized region, until local thermal equilibrium (LTE) is reached, the vibrational energy populations will not adhere to a Boltzmann distribution, thus the N_2^+ emissions will not directly be representative of the O_2 rotational S-branch two-photon transitional line strengths [1]. Additionally, LTE may never be reached in high-enthalpy gas environments, which would render O_2 RIPT measurements invalid. For this study, O_2 RIPT is conducted in a low-enthalpy flow and a lasing pulse width of 10 ns is used, thus the ionized region is assumed to instantaneously be in LTE and the lasing pulse and energy is sufficiently longer than the temporal delay of the electron avalanche ionization and subsequent electron impacted excitation of N_2. O_2 RIPT's N_2^+ photoemission signal is dependent on electron avalanche being the dominant ionization mechanism; it would be of interest to examine how signal strength is affected with shorter laser pulses where multiphoton processes begin to dominate the ionization region.

The measured local gas vibrational temperature via O_2 RIPT is compared at various measurement locations via picosecond vibrational Coherent Anti-Stokes Raman Scattering (ps-CARS). Signal analysis through CARFT reveals theoretical temperature measurements that are close to experimental measurements of O_2 RIPT. The flow regime downstream of the nozzle exit is low enthalpy thus, the molecular vibrational temperatures are assumed to be representative of the total gas temperature enabling a direct comparison between a CFD simulation, CARS, and O_2 RIPT measurements. The CFD and O_2 RIPT measurements show good agreement through the shock structures and diverge slightly once the flow becomes fully-developed. It is shown that O_2 RIPT technique is capable of resolving the temperature fluctuations very closely to those predicted via CFD through the complex shock-interactions and fluid-dynamics downstream of the nozzle exit. Finally, inherent limitations and required gas dynamics are briefly discussed that enable strong O_2 RIPT signal generation and allow the signals to be representative of the excited transition within the rotational branch. Overall, O_2 RIPT is shown to be a promising, novel, thermometry technique that is just beginning to be explored. While demonstrated here in a supersonic regime, it can be used for thermometry applications within any gas medium that contains O_2/N_2 and ideally is not undergoing real-gas effects.

Funding. U.S. Department of Energy (DE-SC0021382); National Science Foundation (2026242).

Acknowledgments. This work is supported by University of Tennessee.

Optics EXPRESS

Disclosures. The authors declare no conflicts of interest.

Data availability. Data underlying the results presented in this paper are not publicly available at this time but may be obtained from the authors upon reasonable request.

Supplemental document. See Supplement 1 for supporting content.

References

1. W. McCord, A. Clark, and Z. Zhang, "One-dimensional air temperature measurements by air resonance enhanced multiphoton Ionization thermometry (ART)," Opt. Express **30**(11), 18539–18551 (2022).
2. T. C. Adamson Jr and J. A. Nicholls, "On the structure of jets from highly underexpanded nozzles into still air," J. Aerospace Sci. **26**(1), 16–24 (1959).
3. P. Behrouzi and J. J. McGuirk, "Underexpanded jet development from a rectangular nozzle with aft-deck," AIAA J. **53**(5), 1287–1298 (2015).
4. E. Franquet, V. Perrier, S. Gibout, and P. Bruel, "Free underexpanded jets in a quiescent medium: A review," Prog. Aeronaut. Sci. **77**, 25–53 (2015).
5. L. Ma, X. Li, S. T. Sanders, A. W. Caswell, S. Roy, D. H. Plemmons, and J. R. Gord, "50-kHz-rate 2D imaging of temperature and H2O concentration at the exhaust plane of a J85 engine using hyperspectral tomography," Opt. Express **21**(1), 1152–1162 (2013).
6. S. Crist, D. Glass, and P. Sherman, "Study of the highly underexpanded sonic jet," AIAA J. **4**(1), 68–71 (1966).
7. J. G. Santiago and J. C. Dutton, "Velocity measurements of a jet injected into a supersonic crossflow," J. Propul. Power **13**(2), 264–273 (1997).
8. M. Gamba, V. Miller, G. Mungal, and R. Hanson, "Combustion characteristics of an inlet/supersonic combustor model," in *50th AIAA aerospace sciences meeting including the new horizons forum and aerospace exposition* (2012), p. 612.
9. D. E. Ogden, K. H. Wohletz, G. A. Glatzmaier, and E. E. Brodsky, "Numerical simulations of volcanic jets: Importance of vent overpressure," J. Geophys. Res.: Solid Earth **113**(B2), B02204 (2008).
10. P. Danehy, J. Weisberger, C. Johansen, D. Reese, T. Fahringer, N. Parziale, C. Dedic, J. Estevadeordal, and B. Cruden, "Non-intrusive measurement techniques for flow characterization of hypersonic wind tunnels," Report NF1676L-31725 (2018).
11. C. Lee and S. Chen, "Recent progress in the study of transition in the hypersonic boundary layer," Natl. Sci. Rev. **6**(1), 155–170 (2019).
12. B. Sun and E. S. Oran, "New principle for aerodynamic heating," Natl. Sci. Rev. **5**(5), 606–607 (2018).
13. K. Avila, D. Moxey, A. D. Lozar, M. Avila, D. Barkley, and B. Hof, "The Onset of Turbulence in Pipe Flow," Science **333**(6039), 192–196 (2011).
14. I. Marusic, D. Chandran, A. Rouhi, M. K. Fu, D. Wine, B. Holloway, D. Chung, and A. J. Smits, "An energy-efficient pathway to turbulent drag reduction," Nat. Commun. **12**(1), 5805 (2021).
15. D. Barkley, B. Song, V. Mukund, G. Lemoult, M. Avila, and B. Hof, "The rise of fully turbulent flow," Nature **526**(7574), 550–553 (2015).
16. X. Wu, P. Moin, J. M. Wallace, J. Skarda, A. Lozano-Durán, and J.-P. Hickey, "Transitional-turbulent spots and turbulent-turbulent spots in boundary layers," Proc. Natl. Acad. Sci. **114**, E5292–E5299 (2017).
17. A. D. Cutler, L. M. Cantu, E. C. Gallo, R. Baurle, P. M. Danehy, R. Rockwell, C. Goyne, and J. McDaniel, "Nonequilibrium supersonic freestream studied using coherent anti-Stokes Raman spectroscopy," AIAA J. **53**(9), 2762–2770 (2015).
18. R. Miles, A. Dogariu, and L. Dogariu, "Localized time accurate sampling of nonequilibrium and unsteady hypersonic flows: methods and horizons," Exp. Fluids **62**(12), 248 (2021).
19. J. P. Slotnick, A. Khodadoust, J. Alonso, D. Darmofal, W. Gropp, E. Lurie, and D. J. Mavriplis, "CFD vision 2030 study: a path to revolutionary computational aerosciences," Report NF1676L-18332 (2014).
20. I. A. Leyva, "The relentless pursuit of hypersonic flight," Phys. Today **70**(11), 30–36 (2017).
21. C. Abram, B. Fond, and F. Beyrau, "Temperature measurement techniques for gas and liquid flows using thermographic phosphor tracer particles," Prog. Energy Combust. Sci. **64**, 93–156 (2018).
22. A. Dogariu, L. E. Dogariu, M. S. Smith, J. Lafferty, and R. B. Miles, "Single shot temperature measurements using coherent anti-Stokes Raman scattering in Mach 14 flow at the Hypervelocity AEDC Tunnel 9," in *AIAA Scitech 2019 Forum* (2019), p. 1089.
23. N. Jiang, M. Webster, W. R. Lempert, J. D. Miller, T. R. Meyer, C. B. Ivey, and P. M. Danehy, "MHz-rate nitric oxide planar laser-induced fluorescence imaging in a Mach 10 hypersonic wind tunnel," Appl. Opt. **50**(4), A20–A28 (2011).
24. M. Boguszko and G. S. Elliott, "On the use of filtered Rayleigh scattering for measurements in compressible flows and thermal fields," Exp. Fluids **38**(1), 33–49 (2005).
25. R. Miles, J. Forkey, and W. Lempert, "Filtered Rayleigh scattering measurements in supersonic/hypersonic facilities," in *28th Joint Propulsion Conference and Exhibit* (1992), p. 3894.
26. R. Miles and W. Lempert, "Two-dimensional measurement of density, velocity, and temperature in turbulent high-speed air flows by UV Rayleigh scattering," Appl. Phys. B **51**(1), 1–7 (1990).
27. J. N. Forkey, N. D. Finkelstein, W. R. Lempert, and R. B. Miles, "Demonstration and characterization of filtered Rayleigh scattering for planar velocity measurements," AIAA J. **34**(3), 442–448 (1996).

Optics EXPRESS

28. K. Gross, R. McKenzie, and P. Logan, "Measurements of temperature, density, pressure, and their fluctuations in supersonic turbulence using laser-induced fluorescence," Exp. Fluids **5**(6), 372–380 (1987).
29. L. S. Chang, C. L. Strand, J. B. Jeffries, R. K. Hanson, G. S. Diskin, R. L. Gaffney, and D. P. Capriotti, "Supersonic mass-flux measurements via tunable diode laser absorption and nonuniform flow modeling," AIAA J. **49**(12), 2783–2791 (2011).
30. A. Farooq, J. B. Jeffries, and R. K. Hanson, "In situ combustion measurements of H2O and temperature near 2.5 μm using tunable diode laser absorption," Meas. Sci. Technol. **19**(7), 075604 (2008).
31. X. Zhou, X. Liu, J. B. Jeffries, and R. Hanson, "Development of a sensor for temperature and water concentration in combustion gases using a single tunable diode laser," Meas. Sci. Technol. **14**(8), 1459–1468 (2003).
32. A. Cutler, P. Danehy, R. Springer, S. O'byrne, D. Capriotti, and R. DeLoach, "Coherent anti-Stokes Raman spectroscopic thermometry in a supersonic combustor," AIAA J. **41**(12), 2451–2459 (2003).
33. M. A. Woodmansee, R. P. Lucht, and J. C. Dutton, "Development of high-resolution N 2 coherent anti-Stokes Raman scattering for measuring pressure, temperature, and density in high-speed gas flows," Appl. Opt. **39**(33), 6243–6256 (2000).
34. S. Roy, J. R. Gord, and A. K. Patnaik, "Recent advances in coherent anti-Stokes Raman scattering spectroscopy: Fundamental developments and applications in reacting flows," Prog. Energy Combust. Sci. **36**(2), 280–306 (2010).
35. A. Bohlin, C. Jainski, B. D. Patterson, A. Dreizler, and C. J. Kliewer, "Multiparameter spatio-thermochemical probing of flame–wall interactions advanced with coherent Raman imaging," Proc. Combust. Inst. **36**(3), 4557–4564 (2017).
36. J. D. Miller, M. N. Slipchenko, J. G. Mance, S. Roy, and J. R. Gord, "1-kHz two-dimensional coherent anti-Stokes Raman scattering (2D-CARS) for gas-phase thermometry," Opt. Express **24**(22), 24971–24979 (2016).
37. J. E. Retter, M. Koll, D. R. Richardson, and S. P. Kearney, "Time-domain self-broadened and air-broadened nitrogen S-branch Raman linewidths at 80–200 K recorded in an underexpanded jet," J. Chem. Phys. **156**(19), 194201 (2022).
38. S. P. Kearney, D. R. Richardson, J. E. Retter, C. E. Dedic, and P. M. Danehy, "Simultaneous temperature/pressure monitoring in compressible flows using hybrid fs/ps pure-rotational CARS," in *AIAA Scitech 2020 Forum* (2020), p. 0770.
39. Z. Zhang, M. Shneider, and R. B. Miles, "Coherent microwave scattering from resonance enhanced multi-photon ionization (radar REMPI): a review," Plasma Sources Sci. Technol. **30**, 103001 (2021).
40. Y. Wu, Z. Zhang, and S. F. Adams, "Temperature sensitivity of molecular oxygen resonant-enhanced multiphoton ionization spectra involving the C3Πgintermediate state," Appl. Phys. B **122**(5), 149 (2016).
41. S. F. Adams, Y. Wu, and Z. Zhang, "Oxygen Rotational Temperature Determination Using Empirical Analyses of C3Π(v′ = 2) ← X3Σ(v″ = 0) Transitions," Appl. Spectrosc. **69**(9), 1036–1041 (2015).
42. J. Sawyer, Y. Wu, Z. Zhang, and S. F. Adams, "O-2 rotational temperature measurements in an atmospheric air microdischarge by radar resonance-enhanced multiphoton ionization," J. Appl. Phys. **113**(23), 233304 (2013).
43. Y. Wu, J. Sawyer, Z. Zhang, and S. F. Adams, "Flame Temperature Measurements by Radar Resonance-Enhanced Multiphoton Ionization of Molecular Oxygen," Appl. Opt. **51**(28), 6864–6869 (2012).
44. P. Linstorm, "NIST chemistry webbook, NIST standard reference database number 69," J. Phys. Chem. Ref. Data Monograph **9**, 1–1951 (1998).
45. A. Alexander, P. Hsu, J. A. Wehrmeyer, S. Roy, J. R. Gord, and J. Kriesel, "Gas-phase temperature measurements at the exhaust of a J85 engine using coherent anti-stokes Raman scattering," in *53rd AIAA Aerospace Sciences Meeting* (2015), p. 1482.
46. S. R. Allmaras and F. T. Johnson, "Modifications and clarifications for the implementation of the Spalart-Allmaras turbulence model," in *Seventh international conference on computational fluid dynamics (ICCFD7)* (2012).
47. R. Palmer, "*The CARSFT Computer Code Calculating Coherent Anti-Stokes Raman Spectra: User and Programmer Information*," (Sandia National Lab., 1989).
48. F. Grisch, P. Bouchardy, and M. Pealat, "CARS studies in hypersonic flows," in *23rd Fluid Dynamics, Plasmadynamics, and Lasers Conference* (1993), p. 3047.
49. D. R. Richardson, S. P. Kearney, and S. J. Beresh, "Femtosecond Coherent Anti-Stokes Raman Spectroscopy in a Cold-Flow Hypersonic Wind Tunnel for Simultaneous Pressure and Temperature Measurements," in *AIAA SCITECH 2022 Forum* (2022), p. 0895.
50. Y. Wu, J. C. Sawyer, L. Su, and Z. Zhang, "Quantitative measurement of electron number in nanosecond and picosecond laser-induced air breakdown," J. Appl. Phys. **119**(17), 173303 (2016).